PAPER

Photocatalytic nanocomposite membranes for environmental remediation

To cite this article: Mahsa Golmohammadi *et al* 2022 *Nanotechnology* **33** 465701

IOP Publishing Nanotechnology
Nanotechnology 33 (2022) 465701 (10pp) https://doi.org/10.1088/1361-6528/ac8682

Photocatalytic nanocomposite membranes for environmental remediation

Mahsa Golmohammadi[1,2], Ali Asghar Sabbagh Alvani[1,2,3,*], Hassan Sameie[2,4], Bastian Mei[4], Reza Salimi[2,4], Dirk Poelman[5] and Federico Rosei[6]

[1] Department of Polymer Engineering & Color Technology, Amirkabir University of Technology, Tehran 1591634311, Iran
[2] Color & Polymer Research Center (CPRC), Amirkabir University of Technology, Tehran 1591634311, Iran
[3] Standard Research Institute (SRI), Karaj, 31745-139, Iran
[4] MESA + Institute for Nanotechnology, Faculty of Science and Technology, University of Twente, Enschede 217, The Netherlands
[5] Department of Solid State Sciences, Lumilab, Ghent University, Krijgslaan 281-S1, 9000 Ghent, Belgium
[6] INRS Centre for Energy, Materials and Telecommunications, 1650 Boul. Lionel Boulet, Varennes, QC J3X 1P7, Canada

E-mail: sabbagh_alvani@aut.ac.ir

Received 29 June 2022, revised 29 July 2022
Accepted for publication 3 August 2022
Published 30 August 2022

Abstract

We report the design and one-pot synthesis of Ag-doped $BiVO_4$ embedded in reduced graphene oxide ($BiVO_4$:Ag/rGO) nanocomposites via a hydrothermal processing route. The binary heterojunction photocatalysts exhibited high efficiency for visible light degradation of model dyes and were correspondingly used for the preparation of photocatalytic membranes using polyvinylidene fluoride (PVDF) or polyethylene glycol (PEG)-modified polyimide (PI), respectively. The surface and cross-section images combined with elemental mapping illustrated the effective distribution of the nanocomposites within the polymeric membranes. Photocatalytic degradation efficiencies of 61% and 70% were achieved after 5 h of visible light irradiation using $BiVO_4$:Ag/rGO@PVDF and $BiVO_4$:Ag/rGO@PI (PEG-modified) systems, respectively. The beneficial photocatalytic performance of the $BiVO_4$:Ag/rGO@PI (PEG-modified) membrane is explained by the higher hydrophilicity due to the PEG modification of the PI membrane. This work may provide a rational and effective strategy to fabricate highly efficient photocatalytic nanocomposite membranes with well-contacted interfaces for environmental purification.

Supplementary material for this article is available online

Keywords: $BiVO_4$, rGO, charge transfer, polymeric membrane, photocatalysis

(Some figures may appear in colour only in the online journal)

1. Introduction

Organic dyes are widely used in industrial processes, such as fabrication of textiles, paper, production of cosmetics, and printing [1]. When dispersed in wastewater, dyes are highly toxic, harmful to aquatic life and continue to be a serious environmental issue. Hence, complete removal is essential before wastewater is discharged into the environment [2]. Unfortunately, many organic dyes are not degradable in conventional wastewater treatment processes due to their complex aromatic molecular structures. In addition, conventional treatment methods are expensive, energy- and time-consuming [3]. Recently, heterogeneous photocatalysis [4–8] has been shown to induce advanced oxidation processes that are effective for wastewater treatment. Yet, to improve process performance, there is growing demand for fabrication of

* Author to whom any correspondence should be addressed.

visible-light-driven photocatalysts and most importantly immobilized photocatalysts [9].

Metal oxides, especially bismuth-based metal oxides have been used [10–12] due to their ability to absorb visible light, non-toxicity, and dispersibility. $BiVO_4$ is characterized by its low band gap energy (2.4 eV) allowing for visible light absorption, non-toxicity, excellent dispersion possibility and good photocatalytic performance under visible light illumination [13, 14]. However, $BiVO_4$ suffers from low carrier mobility [1]. Coupling with a two-dimensional material (such as graphene [15]) and metal doping are two low-cost strategies that have been shown to improve the performance of $BiVO_4$ [14]. Thanks to the high conductivity, large specific surface area ($\sim$2630 $m^2.g^{-1}$) and the abundance of delocalized electrons from the conjugative π-system, coupling of a semiconductor with graphene and reduced graphene oxide (rGO) [16, 17] has been shown to promote charge separation. The single-atom-thick nature of graphene sheets ensures optical transparency, minimizing light shielding-effects. Moreover, favorable absorption properties of $BiVO_4$ when grafted on rGO, were reported [18, 19]. For reducing the band gap, noble metals such as Ag, Au, and Pt can be used in band gap engineering [20]. Ag dopant has been shown to create a mid-gap state thereby modifying the band gap and electronic structure leading to optimized optical properties, visible light harvesting, improve charge kinetics thereby reducing the recombination of photogenerated carriers [21], and interface-surface characteristics [22].

Despite various strategies to enhance photocatalytic properties, using slurry type photocatalytic reactors involves several issues, including the removal of nanoparticles. Due to the small size of the photocatalyst particles and the hazardous side effects of nanoparticles dispersed in water, removal is mandatory [23–25]. In recent years, embedding photocatalytic nanoparticles in polymeric membranes has been reported as a feasible approach to address the drawbacks of slurry reactors [26]. The effectiveness of the polymeric membrane is known to be affected by both fouling and the deposition of contaminants on the membranes boundary layer which is known as concentration polarization; so that photocatalytic membranes are predicted to suffer from undesirable photocatalytic degradation efficiency [27, 28].

Specifically, it is suggested that photocatalytic nanoparticles immobilized at the outer membrane surface reduce fouling, while embedded nanoparticles primarily participate in the degradation of wastewater contaminants [27]. For example, Ramasundaram *et al* fabricated TiO_2/PI films and reported its performance for the degradation of amoxicillin, atrazine and 4-chlorophenol [29]. The modified membrane was shown to provide high thermal and oxidative stability, revealing the potential of PI for use in photocatalytic membranes [29]. Moreover, Biswas *et al* prepared a $BiVO_4$-GO-PVDF membrane and successfully used it for the degradation of methylene blue (MB). Their results indicate that $BiVO_4$-GO-PVDF remains photocatalytically active for the degradation of MB, Rhodamine B and Safranin-O [30]. Recently, we investigated Ag-functionalized $Bi_2W(Mo)O_6$/PVDF membranes for photocatalytic water treatment and obtained a degradation rate of 51% with the as-prepared photocatalytic membrane for MB [31].

Despite the growing interest in photocatalytic membranes, a good comparison of different types of polymers has not yet been reported. Moreover, membrane surface modification by means of hydrophilic layers has not yet been addressed.

Here we report on the performance of $BiVO_4$-based photocatalysts embedded in photocatalytic membranes using PI and PVDF as relevant polymers. Specifically, we designed and fabricated $BiVO_4$:Ag/rGO to tackle the inherent slow electron–hole pair migration of $BiVO_4$. Moreover, the influence of hydrophilic layers has been addressed by PEG modification. The photocatalytic experiments performed suggest that PI-based membranes are more suitable for wastewater treatment due to both the modified hydrophilicity (favorable wettability) and higher porosity which permit contact between the photocatalytic membrane and the dye solution.

2. Experimental methods

2.1. Synthesis of $BiVO_4$ based photocatalysts

Bismuth (III) nitrate pentahydrate ($Bi(NO_3)_3.5H_2O$), ammonium meta-vanadate (NH_4VO_3), silver nitrate ($AgNO_3$) and all other reagents were of analytical grade (Sigma-Aldrich) and used without further purification. Graphene oxide (GO) was synthesized from natural graphite powder through a modified Hummers method following previous reports [32]. The $BiVO_4$/rGO nanocomposite was fabricated via a facile hydrothermal process. Briefly, 40 mg GO was dispersed in 40 ml deionized water by ultrasonication to obtain a homogeneous suspension. 0.1796 g $Bi(NO_3)_3.5H_2O$ and 0.0430 g NH_4VO_3 were separately added to two solutions of absolute ethanol (10 ml) while stirring for at least 30 min at room temperature. Subsequently, all solutions were combined. The pH was adjusted to a pH of 8.0 using a 25 vol% ammonia solution. After stirring for 30 min, a stable bottle-green colored slurry was obtained. The resulting mixture was transferred to a 100 ml Teflon-lined stainless-steel autoclave and heated to 180 °C for 6 h under autogenous pressure. The reaction mixture was allowed to cool down to room temperature and the precipitate was filtered, washed five times with distilled water and dried in vacuum oven at 60 °C for 12 h. The obtained powered was labeled as $BiVO_4$/rGO. For comparison, the same method was repeated to synthesize pure $BiVO_4$ without adding GO to the mixture.

$BiVO_4$:Ag was prepared as follows; 0.44 g of $Bi(NO_3)_3.5H_2O$ and 0.108 g of NH_4VO_3 were separately added to two solutions of absolute ethanol (25 ml) while stirring for at least 30 min at room temperature. Additionally, 0.0023 g of $AgNO_3$ (Ag/Bi was 0.5 wt%) was dissolved in 5 ml deionized water. The three solutions were mixed while stirring and subsequently the pH was adjusted to pH 8.0 with an ammonia solution at 25% and stirred for 30 min. The final solution was transferred to a 100 ml Teflon-lined

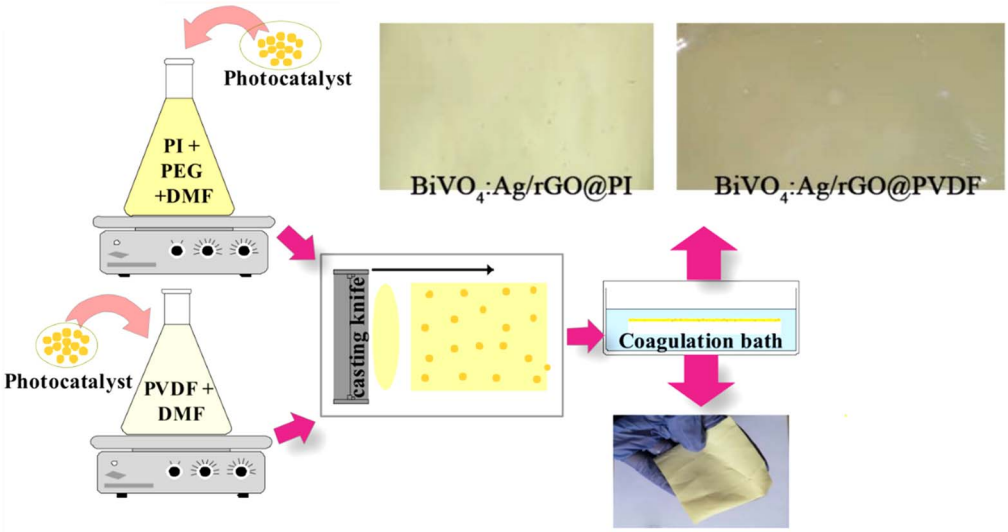

Figure 1. Schematic illustration of PVDF and PI membranes preparation process.

stainless-steel autoclave and heated to 180 °C for 6 h under autogenous pressure. The reaction mixture was cooled, washed and dried as mentioned in the previous synthesis. This product was labeled as $BiVO_4$:Ag. For the synthesis of $BiVO_4$:Ag/rGO, a ratio of $BiVO_4$ to GO of 3:1 was chosen [30] and the individual preparation steps outlined above were followed to obtain $BiVO_4$:Ag/rGO.

2.2. Preparation of the photocatalytic membranes

Polyvinylidene fluoride (PVDF), polyimide (PI), polyethylene glycol 400 (PEG 400) and dimethylformamide (DMF) were purchased from Sigma-Aldrich and used without further purification. The PVDF and PI membranes were prepared using the phase inversion method [33]. Generally, for the preparation of the photocatalytic membranes a mass ratio of $r = m_n/m_p$, in which m_n and m_p are nanoparticle mass and polymer mass respectively, lower than the critical ratio of $r* \approx 0.2$ to 0.3 was chosen to avoid polymer/nanoparticle agglomeration. Using out of the optimum m_n/m_p concentration leads to the agglomeration formation, which hinders both the light penetration into the membrane and light irradiation on the photocatalysts that are existed inside of the membrane layer and severe blocking of light penetration. To remove possible moisture, PVDF and PI powders were dried in a vacuum oven at 40 °C for 24 h. A mixture of 2.3 g PVDF and 10 ml DMF was stirred at 30 ± 5 °C for 24 h and subsequently degassed overnight in a vacuum oven. Then, 0.69 g $BiVO_4$:Ag/rGO photocatalyst powder was added to the obtained solution and stirred for 24 h. For the fabrication of $BiVO_4$:Ag/rGO-modified PI membranes, a mixture of 8.5 g PI, 2.125 g PEG (25% [34]) and 60 ml DMF was stirred at 30 ± 5 °C for 24 h and degassed overnight. Afterwards, 2.55 g $BiVO_4$:Ag/rGO was added to the obtained solution and stirred for 1 h. Finally, the blend solutions of PI and PVDF were cast on a glass plate using a casting knife set at a gap of 200 μm and immediately immersed into a coagulation bath (distilled water) for 30 min to induce phase inversion and to form free films of PVDF and PI membranes. Figure 1 illustrates schematically all the preparation steps of PVDF and PI membranes.

2.3. Materials characterization

X-ray powder diffraction (XRD, Equinox 3000, Intel) was used to examine the phases of samples using Cu K_α radiation ($\lambda = 1.541874$ Å) and scanning range from 10° to 80° at a scanning rate of 6° min^{-1} and a step size of 0.02°. Scanning electron microscopy (SEM, SERON Technology, AIS2100) and diffuse reflectance spectroscopy (DRS, Avaspec-2048-TEC) were used to image sample morphology and determining the absorbance and band gap of the samples, respectively. Functional groups were determined by Fourier transform infrared (FTIR, Perkin Elmer FTIR Spectrum 100) and Raman spectroscopy (Teksan, Takram using a 532 nm laser at 10 mW incident power for excitation). Surface area measurements were performed using a QUANTACHROME Autosorb-1-mp instrument. Field emission SEM (FESEM, TESCAN model MIRA III equipped with SAMX detector for energy-dispersive x-ray spectroscopy, France) was used to examine the surface and cross-section of the prepared membranes as well as the elemental distribution. Static contact angle measurements were obtained using a contact angle goniometer (Jikan CAG-20).

2.4. Photocatalytic activity measurements

The photocatalytic activity of the as-prepared pure $BiVO_4$, $BiVO_4$/rGO, and $BiVO_4$:Ag and $BiVO_4$:Ag/rGO nanocomposites were evaluated by MB degradation. All experiments were performed using visible-light irradiation obtained with a 500 W Halogen lamp (450–700 nm, OSRAM GmbH, Germany) in a quartz photoreactor fitted with a circulation cooling system to maintain a constant temperature. The as-prepared photocatalysts (50 mg) were suspended in 100 ml of 10 $mg.l^{-1}$ MB aqueous solution. Before illumination, the suspension was magnetically stirred for 60 min in the dark to

reach an adsorption–desorption equilibrium between MB and the photocatalyst.

At given irradiation time intervals, samples from the aqueous solution were collected and subsequently centrifuged to remove the particles. Then, the absorption spectra of the prepared photocatalysts were measured using UV–vis spectroscopy (JENWAY 6715, 380–800 nm). The MB concentration was analyzed by measuring the maximum absorption at 665 nm. The degradation efficiency of MB was calculated using equation (1) [35]:

$$\eta = \frac{C_0 - C_t}{C_0} = \frac{A_0 - A}{A_0} \times 100\%, \quad (1)$$

where C_0 and A_0 are the initial concentration and absorbance of the MB solution at 665 nm; C_t and A are the concentration and absorbance of the MB solution at 665 nm at time t.

Similarly, the photocatalytic activity of the photocatalyst/membrane has been measured in a cylindrical membrane reactor (figure S1 (available online at stacks.iop.org/NANO/33/465701/mmedia)). A photocatalytic membrane reactor (PMR) with an absolute volume of 1 l and equipped with two 500 W Halogen lamps (450–700 nm, OSRAM GmbH, Germany) was used to study the photocatalytic MB degradation. The prepared rectangle flat sheet photocatalytic membrane (200×100 mm^2 in size) was placed at the center of the PMR. The lamp, which was placed in a double layer quartz (for its protection in aqueous environment) was irradiated from both sides of the immersed membrane. At specific time intervals, the optical absorption from the MB solution were analyzed by UV–vis spectrophotometer at 665 nm. Finally, the degradation efficiency of photocatalytic membranes was calculated using equation (1).

3. Results and discussion

3.1. Photocatalyst characterization

The phase, the crystallinity and the structural composition of the as-prepared samples (pure $BiVO_4$, $BiVO_4$:Ag, $BiVO_4$/rGO, $BiVO_4$:Ag/rGO) were investigated by XRD. As shown in figure 2(a), all XRD patterns have sharp and well-defined peaks and phase-impurities are not observed. Generally, the patterns match the tetragonal scheelite $BiVO_4$ phase according to JCPDS No. 078–1535. The crystal structure of tetragonal scheelite $BiVO_4$ and corresponding polyhedron structure are shown in figure 2(b). The crystal structure of tetragonal $BiVO_4$ scheelite is similar to monoclinic $BiVO_4$ scheelite because both possess in both cases the BiO_8 dodecahedra and VO_4 tetrahedra have corner-sharing connection [36]. $BiVO_4$ structures in figure 2(b) were visualized using the *VESTA* package [37]. *GSAS* software [38] was used for $BiVO_4$ and $BiVO_4$:Ag crystal structure refinement and study of crystallographic characterization. The results are shown in figure S2 along with an extended discussion of all XRD data obtained. The lattice parameters and phase analysis of mass fraction (weight %) of both pure $BiVO_4$ and Ag-doped $BiVO_4$ are summarized in table S1.

Raman spectroscopy confirmed the nature of GO (figure S3) and the structure of the $BiVO_4$/rGO and $BiVO_4$:Ag/rGO nanocomposites (see figure 2(c) and additional discussion in SI). The surface morphology and composition of the GO and photocatalysts were imaged by SEM (figure S4). After rGO deposition, the BET surface areas of $BiVO_4$:Ag and $BiVO_4$:Ag/rGO increased to 13.96 and 30.85 m^2 g^{-1}, respectively. Since the surface area correlates with the photocatalytic activity, it is expected to observe an enhancement in the photocatalytic activity of $BiVO_4$:Ag/rGO composite compared to the $BiVO_4$:Ag. Table S2 summarizes the elemental composition of the pure $BiVO_4$ and $BiVO_4$:Ag samples as identified by EDS and revealing the concentration of Bi, V and O elements, with presence of Ag in $BiVO_4$:Ag composite (figure S5 along with the discussion provided in SI). Finally, UV–vis DRS was employed to determine the optical property of the photocatalysts. The pure $BiVO_4$, $BiVO_4$:Ag and $BiVO_4$:Ag/rGO nanocomposite exhibit an absorption edge at around 566, 593 and 620 nm, respectively (figure S6). The optical band gap energy (E_g) of the obtained samples was estimated using a Tauc plot [39] (figure 2(d)). The approximate band gaps of $BiVO_4$, $BiVO_4$:Ag and $BiVO_4$:Ag/rGO are 2.29, 2.09 and 2.00 eV, respectively. Finally, the FT-IR spectra of pure $BiVO_4$, $BiVO_4$:Ag, $BiVO_4$/rGO and $BiVO_4$:Ag/rGO are shown in figure S7 with accompanying text in the SI.

3.2. Photocatalytic membrane characterization

The photocatalytic performance of PVDF photocatalytic membranes is a topic of recent interest [31]. Here we report a comparison of the photocatalytic performance of the PVDF membrane with another oxidation-resistant membrane, PEG-modified PI. In the following, we discuss the results of immobilizing of $BiVO_4$:Ag/rGO nanocomposites into/onto the PVDF and PEG-modified PI membranes and their photocatalytic performances.

FESEM images of the top surface (figures 3(a)–(b)) and the cross-section (figures 3(c)–(d)) of the $BiVO_4$:Ag/rGO@PI (PEG-modified) and the top surface (figures 3(e)–(f)) and the cross-section (figures 3(g)–(h)) of the $BiVO_4$:Ag/rGO@PVDF including the related elemental mapping results are shown in figure 3. The comparison of surface images shows a clear difference in morphology, elemental distribution and pore sizes of the membrane samples. Specifically, PI-based membranes appear to be less dense, contain generally larger pores and a good photocatalyst distribution is obtained. Several studies have reported that the uniform elemental distribution of photocatalysts across the photocatalytic membranes improves the wastewater treatment efficiency significantly. Because photocatalyst aggregation on the surface of the membrane may hinder the performance of photocatalyst and decrease both the surface area and photocatalytic active sites in the photocatalytic dye degradation [40]. Moreover, a denser membrane structure as observed for $BiVO_4$:Ag/rGO@PVDF membrane might lead to low light penetration and inactive $BiVO_4$:Ag/rGO nanocomposites inside the membrane thereby decreasing the performance of

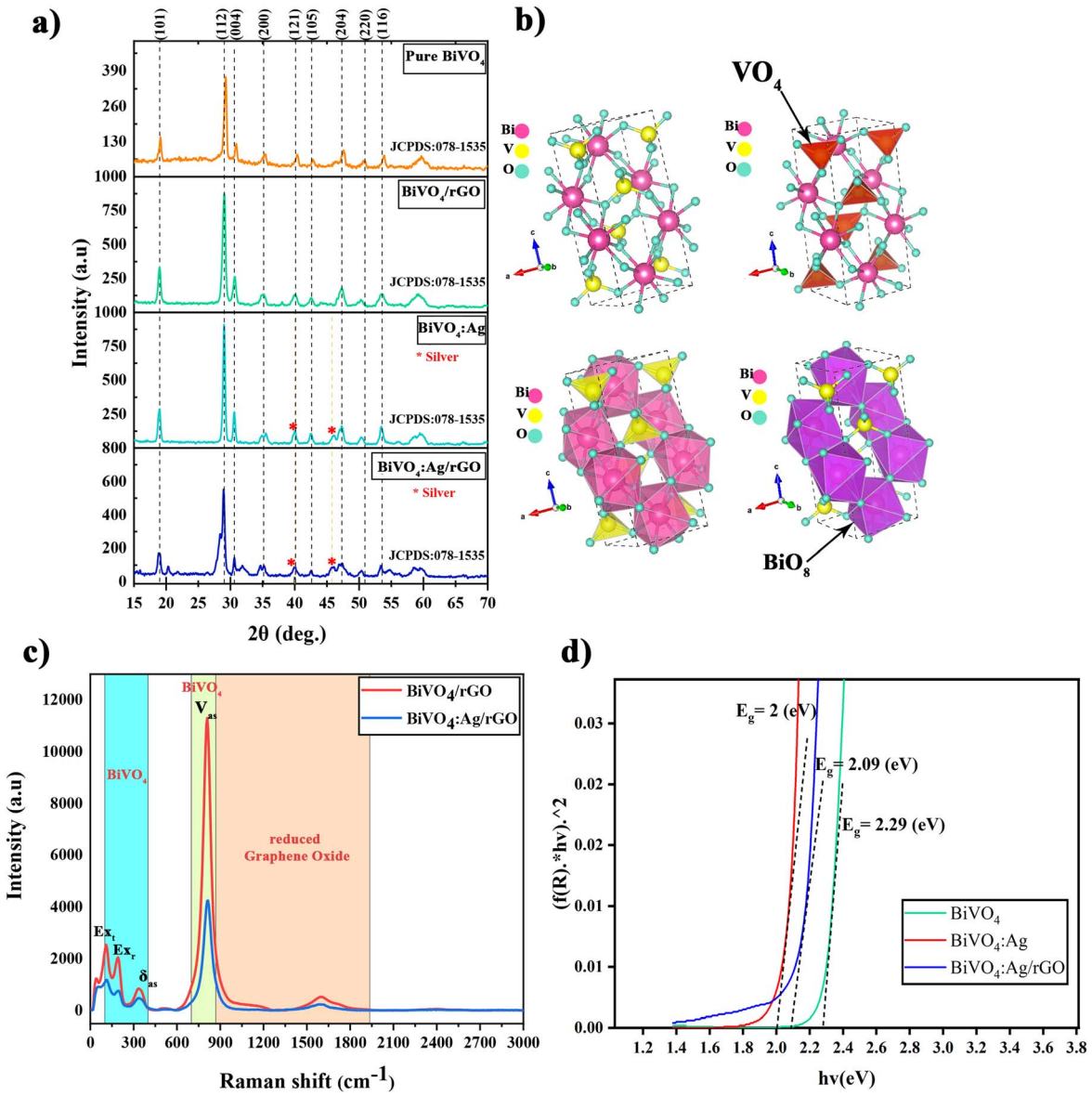

Figure 2. (a) X-ray diffraction (XRD) patterns of $BiVO_4$, $BiVO_4$/rGO, $BiVO_4$:Ag and $BiVO_4$:Ag/rGO samples, (b) the crystal structure of tetragonal scheelite $BiVO_4$ and corresponding polyhedron structure (VO_4 tetrahedra in red and BiO_8 dodecahedra in purple), (c) Raman spectra of $BiVO_4$/rGO and $BiVO_4$:Ag/rGO and (d) Tauc plot from diffuse reflectance spectroscopy of $BiVO_4$, $BiVO_4$:Ag and $BiVO_4$:Ag/rGO.

the BiVO4:Ag/rGO@PVDF membrane. Thus, it is expected that $BiVO_4$:Ag/rGO@PI (PEG-modified) membranes show better photocatalytic performance in comparison with the $BiVO_4$:Ag/rGO@PVDF.

Besides, the photocatalyst elemental distribution on the surface, the distribution throughout the membrane is of importance, because of their effective anti-fouling role that increases the performance of the photocatalytic membrane. Elemental mapping (Bi and Ag) of the cross-section and top surface of both $BiVO_4$:Ag/rGO@PVDF and $BiVO_4$:Ag/rGO@PI (PEG-modified) membranes was performed, as shown in figure 3. Elemental mapping confirms the silver doping of $BiVO_4$. In addition, by comparison of the elemental maps of silver and bismuth, it can be concluded that $BiVO_4$:Ag/rGO nanocomposites are uniformly dispersed cross the prepared membranes. The good distribution is likely induced by a suitable electrostatic interaction between the photocatalytic nanocomposites and the polymeric membranes. Full elemental maps (F, O, C, V and N) of any other atoms present in the material are provided in figure S8.

The photocatalytic performance of the as-prepared photocatalysts (figure 4(a)) and $BiVO_4$:Ag/rGO@PVDF and $BiVO_4$:Ag/rGO@PI (PEG-modified) membranes (figure 4(b)) for MB degradation under visible light are summarized in figure 4. To achieve adsorption–desorption equilibrium, the dye suspension was magnetically stirred for 60 min in the dark before illumination. The MB degradation efficiency of $BiVO_4$:Ag/rGO (83%) was found to be higher than for other photocatalysts. This phenomenon is attributed to the band gap engineering by Ag doping and rGO decoration which leads to

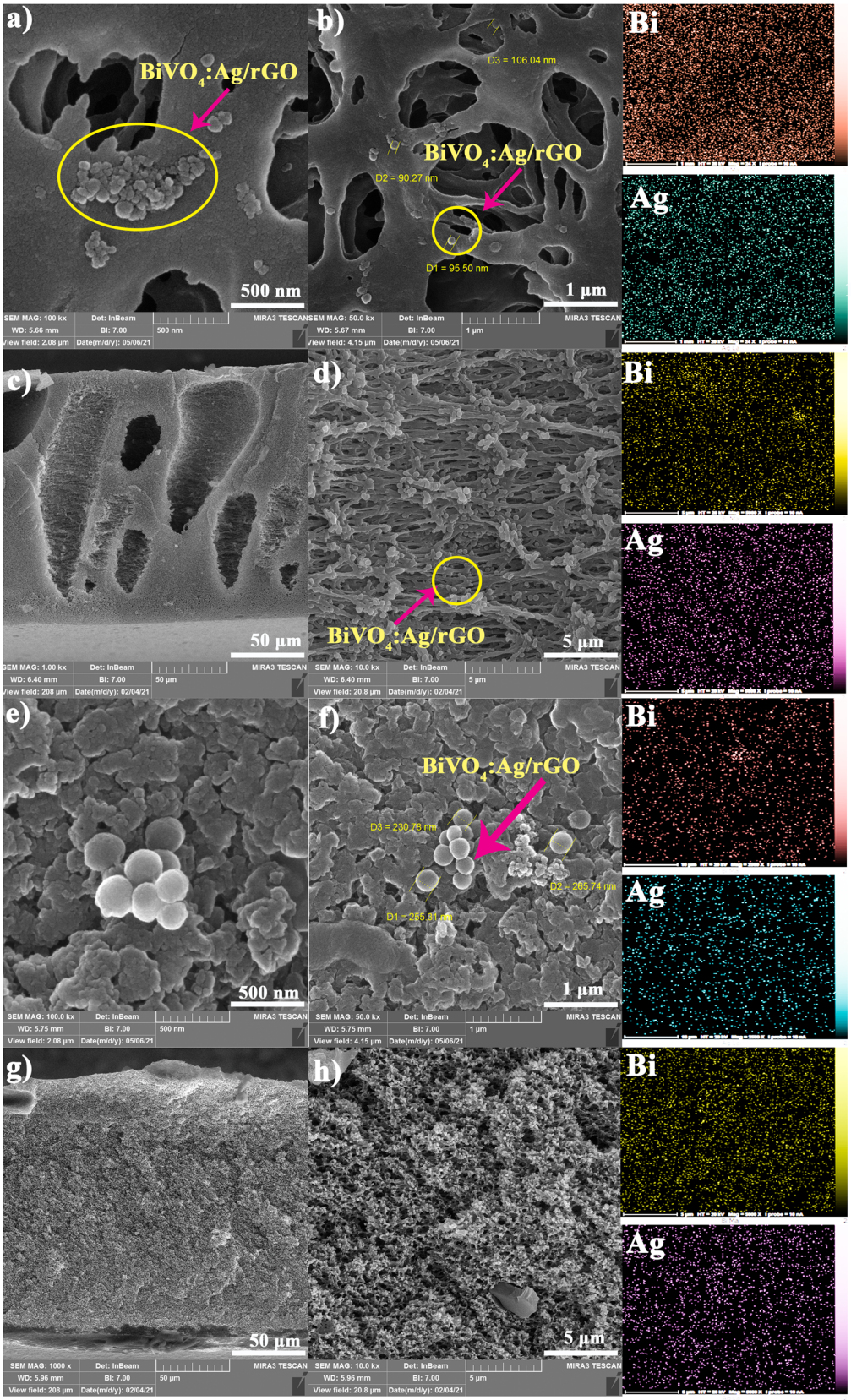

Figure 3. (a)–(b) FESEM images of the top surface, (c)–(d) cross-section images of $BiVO_4$:Ag/rGO@PI (PEG-modified) membrane, (e)–(f) FESEM images of the top surface and (g)–(h) cross-section images of $BiVO_4$:Ag/rGO@PVDF membrane with related elemental map distribution of Bi and Ag.

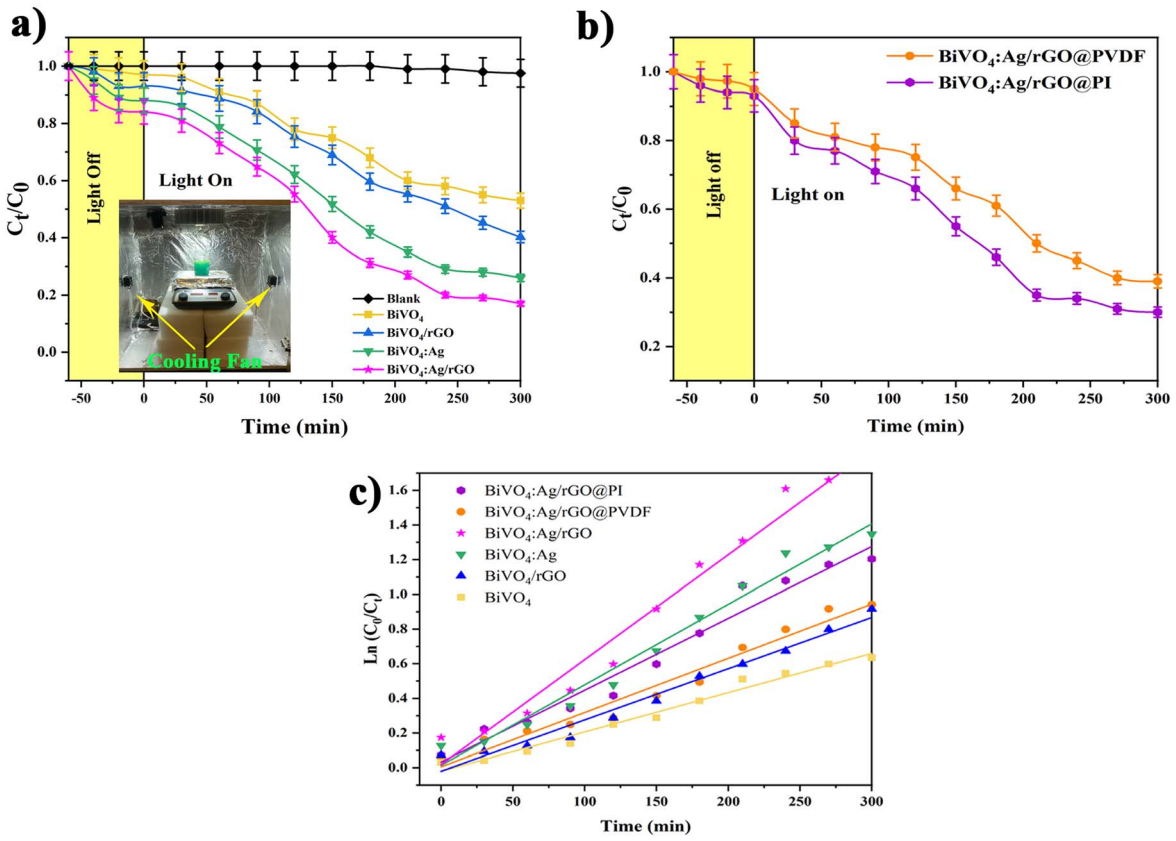

Figure 4. Photocatalytic degradation of MB in the dark and under visible light irradiation in the presence of, (a) photocatalysts: $BiVO_4$ pure, $BiVO_4$:Ag, $BiVO_4$/rGO and $BiVO_4$:Ag/rGO, (b) $BiVO_4$:Ag/rGO@PI (PEG-modified) and $BiVO_4$:Ag/rGO@PVDF membranes; (c) MB degradation kinetic curves of ln (C_0/C_t) versus time for different photocatalysts and $BiVO_4$:Ag/rGO@PI (PEG-modified) and $BiVO_4$:Ag/rGO@PVDF membranes.

enhancement in both visible light absorption and separation of photoinduced charge carriers, ultimately enhancing the photocatalytic performance of $BiVO_4$:Ag/rGO nanocomposites.

The photocatalytic efficiency of $BiVO_4$:Ag/rGO@PVDF and $BiVO_4$:Ag/rGO@PI (PEG-modified) membranes after 300 min are 61% and 70%, respectively. The first-order MB photocatalytic degradation rates determined from as-prepared photocatalysts are summarized in figure 4(c). The rate constants were obtained by fitting the experimental data using equation (2):

$$\ln (C_t/C_0) = -k\, t, \tag{2}$$

where C_t/C_0 and k are the ratio of the concentration of MB solution at adsorption–desorption equilibrium and first-order rate constant in min^{-1}. Accordingly, the kinetic constants for pure $BiVO_4$, $BiVO_4$/rGO, and $BiVO_4$:Ag and $BiVO_4$:Ag/rGO were obtained as 0.0023, 0.0030, 0.0047, and 0.0061 min^{-1}, respectively (figure 4(c)). Moreover, the kinetic constants for $BiVO_4$:Ag/rGO@PVDF and $BiVO_4$:Ag/rGO@PI (PEG-modified) membranes are 0.0031 min^{-1} and 0.0040 min^{-1}, respectively (figure 4(c)). As such, both prepared photocatalytic membranes can be suitable candidates for environmental-friendly photocatalytic degradation processes. A possible mechanism of photocatalytic degradation of MB over $BiVO_4$:Ag/rGO@PI (PEG-modified) membrane is sketched in figure S9.

To explore the differences in the activity, the wettability of the surface of the polymeric membranes was determined [41] using static water droplet contact angle measurements to obtain the membrane surface hydrophilicity (θ_a). The water contact angle measurements of pure PI, $BiVO_4$:Ag/rGO@PI (PEG-modified), pure PVDF and $BiVO_4$:Ag/rGO@PVDF membranes and their related images are shown in figure 5. PEG-modified PVDF membranes have been excluded in this study as PVDF is not miscible with PEG (as a modification additive to obtain a mixed matrix membrane). Moreover, the contact angle of the PI membrane (without PEG) prepared via phase inversion method is well-known from literature and has been reported to be 92° [42], previously. The hydrophilic PEG used in PI modification was responsible for the hydrophilicity enhancement resulting in a contact angle of 77°. This confirmed the PEG modification role in the increasing of the membrane surface hydrophilicity. Moreover, the lower contact angle of the PI-membrane was also maintained for $BiVO_4$:Ag/rGO@PI (PEG-modified) sample. Nevertheless, for both membranes a significant decrease in contact angle was observed. A contact angle of 70.9° was obtained in the case of the loaded PVDF-membrane, whereas for the loaded PI-membrane an angle of 66.3° was obtained. The observed

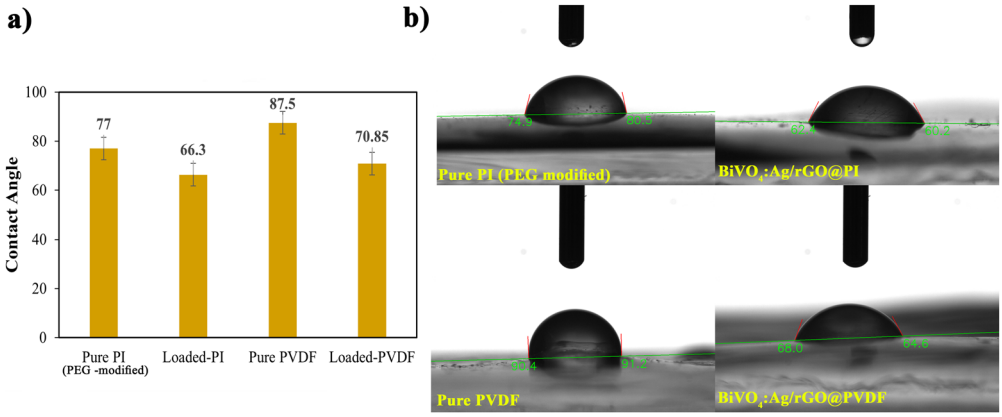

Figure 5. (a) Characterizations of hydrophilicity of the different PI and PVDF membranes and (b) water contact angle of the membrane surface.

decrease is likely related to the enhanced surface roughness and the wettability of the photocatalyst itself [43].

Besides its favorable hydrophobicity, the slightly lower efficiency of PVDF-based membranes is likely related to the partial coverage of the photocatalysts by the polymeric membranes and consequently, the contact of the photocatalytic nanocomposites with the dye is minimized. PI membranes with larger porosity allow for a better contact between wastewater and the active photocatalytic nanocomposite embedded inside and at the surface of the membrane. As shown by the obtained results, for the design of photocatalytic membranes, four main factors should be considered carefully; (I) type of the selected membrane; (II) optimum mass ratio of loaded photocatalyst, (III) preparation method and (IV) effect of the surface modification. This ultimately leads to higher photocatalytic performance of PI-based membranes.

Since both prepared flat sheets are fixed photocatalytic membranes (without any permeation), other water treatment parameters (e.g. rejection rate of dye solution) which are considered for permeable photocatalytic membranes are not applicable here and therefore have not been determined.

4. Conclusions and perspectives

In this work, an improved $BiVO_4$:Ag/rGO nanocomposite was synthesized using *in situ* deposition of Ag dopants and GO reduction by a hydrothermal method. The $BiVO_4$:Ag/rGO nanocomposite, compared with pure $BiVO_4$, $BiVO_4$/rGO and $BiVO_4$:Ag samples, exhibits tangible enhancement in photocatalytic activity due to the band gap narrowing of Ag dopants and electron transfer facilitation of rGO sheets. Since $BiVO_4$:Ag/rGO@PVDF membrane has a denser structure, it has low light penetration that leads to a less effective photocatalytic activity rather than $BiVO_4$:Ag/rGO@PI (PEG-modified). Moreover, the contact angle value or hydrophilicity of the $BiVO_4$:Ag/rGO@PI (PEG-modified) and $BiVO_4$:Ag/rGO@PVDF are 66.3° and 70.9°, respectively, which better photocatalytic degradation performance is expected from the first membrane due to the higher hydrophilicity. For PVDF and PI photocatalytic membranes prepared by loading of $BiVO_4$:Ag/rGO nanocomposite, a MB degradation efficiency of approx. 70% was obtained using $BiVO_4$:Ag/rGO@PI (PEG-modified) (after 300 min visible light irradiation), compared with a MB degradation efficiency of 61% for PVDF-based membranes. The performance of the PI membrane has been primarily assigned to its favorable hydrophilicity and open structure. These observations point to future directions for the design and synthesis of high-performance photocatalytic membranes for wastewater treatment applications.

Data availability statement

No new data were created or analysed in this study.

Conflicts of interest

The authors declare no conflicts of interest.

ORCID iDs

Mahsa Golmohammadi https://orcid.org/0000-0003-3347-5734
Ali Asghar Sabbagh Alvani https://orcid.org/0000-0003-1986-5285
Hassan Sameie https://orcid.org/0000-0003-0374-880X
Bastian Mei https://orcid.org/0000-0002-3973-9254
Reza Salimi https://orcid.org/0000-0003-1218-6706
Dirk Poelman https://orcid.org/0000-0002-3930-172X
Federico Rosei https://orcid.org/0000-0001-8479-6955

References

[1] Carmen Z and Daniela S 2012 Textile organic dyes—characteristics, polluting effects and separation/elimination procedures from industrial effluents—a critical overview *Text. Org. Dye* **1** 55–86

[2] Ghaly A E, Ananthashankar R, Alhattab M and Ramakrishnan V V 2013 Production, characterization and treatment of textile effluents: a critical review *J. Chem. Eng. Process Technol.* **05** 1–18

[3] Shi Q, Zhao W, Xie L, Chen J, Zhang M and Li Y 2016 Enhanced visible-light driven photocatalytic mineralization of indoor toluene via a BiVO4/reduced graphene oxide/Bi_2O_3 all-solid-state Z-scheme system *J. Alloys Compd.* **662** 108–17

[4] Brüninghoff R, Van Duijne A K, Braakhuis L, Saha P, Jeremiasse A W, Mei B and Mul G 2019 Comparative analysis of photocatalytic and electrochemical degradation of 4-ethylphenol in saline conditions *Environ. Sci. Technol.* **53** 8725–35

[5] Karuppannan R, Mohan S and Do T-O 2021 Amine-functionalized metal–organic framework integrated bismuth tungstate (Bi2WO6/NH2-UiO-66) composite for the enhanced solar-driven photocatalytic degradation of ciprofloxacin molecules *New J. Chem.* **45** 22650–60

[6] Pirhashemi M, Habibi-Yangjeh A and Rahim Pouran S 2018 Review on the criteria anticipated for the fabrication of highly efficient ZnO-based visible-light-driven photocatalysts *J. Ind. Eng. Chem.* **62** 1–25

[7] Yu H *et al* 2021 Synergy of ferroelectric polarization and oxygen vacancy to promote CO2 photoreduction *Nat. Commun.* **12** 1–10

[8] Salimi R, Sabbagh Alvani A A, Mei B T, Naseri N, Du S F and Mul G 2019 Ag-Functionalized $CuWO_4/WO_3$ nanocomposites for solar water splitting *New J. Chem.* **43** 2196–203

[9] Kong D, Ruan X, Geng J, Zhao Y, Zhang D, Pu X, Yao S and Su C 2021 0D/3D $ZnIn_2S_4/Ag_6Si_2O_7$ nanocomposite with direct Z-scheme heterojunction for efficient photocatalytic H_2 evolution under visible light *Int. J. Hydrog. Energy* **46** 28043–52

[10] Walid A, Soeparman S, Wahyudi S and Sasongko M N 2021 The effect of nickel doped bismuth vanadium oxide on microstructures and electric properties towards BiVO4-NiO composite *Mater. Chem. Phys.* **265** 124452

[11] Malathi A, Vasanthakumar V, Arunachalam P, Madhavan J and Ghanem M A 2017 A low cost additive-free facile synthesis of $BiFeWO_6/BiVO_4$ nanocomposite with enhanced visible-light induced photocatalytic activity *J. Colloid Interface Sci.* **506** 553–63

[12] Yao X, Zhen H, Zhang D, Liu J, Pu X and Cai P 2022 Microwave-assisted hydrothermal synthesis of broadband Yb^{3+}/Er^{3+} co-doped $BiOI/Bi_2O_4$ photocatalysts with synergistic effects of upconversion and direct Z-scheme heterojunction *Colloids Surf.* A **648** 129276

[13] Liang Y, Tsubota T, Mooij L P A and van de Krol R 2011 Highly improved quantum efficiencies for thin film $BiVO_4$ photoanodes *J. Phys. Chem.* C **115** 17594–8

[14] Tan H L, Amal R and Ng Y H 2017 Alternative strategies in improving the photocatalytic and photoelectrochemical activities of visible light-driven $BiVO_4$: a review *J. Mater. Chem.* A **5** 16498–521

[15] Sameie H, Alvani A A S, Mei B T, Salimi R, Poelman D and Rosei F 2021 Mo-doped ZnV_2O_6/reduced graphene oxide photoanodes for solar hydrogen production *Electrochim. Acta* **382** 138333

[16] Dimiev A M and Eigler S 2016 *Graphene Oxide : Fundamentals and Applications* (New York: Wiley)

[17] Jones B M F, Mamba G, Ansari S A, Maruthamani D, Muthuraj V and Nkambule T T I 2021 Simple fabrication and unprecedented visible light response of $NiNb_2O_6$/RGO heterojunctions for the degradation of emerging pollutants in water *New J. Chem.* **45** 22697–713

[18] Xiang Q, Yu J and Jaroniec M 2012 Graphene-based semiconductor photocatalysts *Chem. Soc. Rev.* **41** 782–96

[19] Wang T, Li C, Ji J, Wei Y, Zhang P, Wang S, Fan X and Gong J 2014 Reduced graphene oxide (rGO)/$BiVO_4$ composites with maximized interfacial coupling for visible lght photocatalysis *ACS Sustain. Chem. Eng.* **2** 2253–8

[20] Kowalska E, Wei Z and Janczarek M 2018 Band-gap engineering of photocatalysts: surface modification versus doping *Visible-Light-Active Photocatalysis: Nanostructured Catalyst Design, Mechanisms, and Applications* (Germany: wiley) **16** 447–84

[21] Chauhan N, Singh V, Kumar S and Sirohi K 2019 Preparation of palladium, silver, and nitrogen co-doped mesoporous titanium dioxide nanoparticles to investigate their photocatalytic action *Mater. Res. Express* **6** 1150e7

[22] Umezawa N and Ye J 2012 Role of complex defects in photocatalytic activities of nitrogen-doped anatase TiO_2 *Phys. Chem. Chem. Phys.* **14** 5924–34

[23] Corredor J, Perez-Peña E, Rivero M J and Ortiz I 2020 Performance of rgo/tio_2 photocatalytic membranes for hydrogen production *Membranes (Basel)* **10** 1–13

[24] Shi H, Magaye R, Castranova V and Zhao J 2013 Titanium dioxide nanoparticles: a review of current toxicological data *Part. Fibre Toxicol.* **10** 1–33

[25] Zhang D, Liu X, Wang S, Fan B, Shao Z, Su C and Pu X 2021 Enhanced charges separation to improve hydrogen production efficiency by organic piezoelectric film polarization *J. Alloys Compd.* **869** 159390

[26] Kuttiani Ali J, Maher Chabib C, Abi Jaoude M, Alhseinat E, Teotia S, Patole S, Hussain Anjum D and Qattan I 2021 Enhanced removal of aqueous phenol with polyimide ultrafiltration membranes embedded with deep eutectic solvent-coated nanosilica *Chem. Eng. J.* **408** 128017

[27] Zakria H S, Othman M H D, Kamaludin R, Sheikh Abdul Kadir S H, Kurniawan T A and Jilani A 2021 Immobilization techniques of a photocatalyst into and onto a polymer membrane for photocatalytic activity *RSC Adv.* **11** 6985–7014

[28] Karimi A, Khataee A, Vatanpour V and Safarpour M 2019 High-flux PVDF mixed matrix membranes embedded with size-controlled ZIF-8 nanoparticles *Sep. Purif. Technol.* **229** 115838

[29] Ramasundaram S, Seid M G, Lee W, Kim C U, Kim E J, Hong S W and Choi K J 2017 Preparation, characterization, and application of TiO_2-patterned polyimide film as a photocatalyst for oxidation of organic contaminants *J. Hazard. Mater.* **340** 300–8

[30] Biswas M R U D and Oh W-C 2018 Synthesis of $BiVO_4$-GO-PVDF nanocomposite: an excellent, newly designed material for high photocatalytic activity towards organic dye degradation by tuning band gap energies *Solid State Sci.* **80** 22–30

[31] Mortazavi Milani H, Sabbagh Alvani A A, Salimi R, Sameie H and Poelman D 2021 Ag-functionalized Bi2W (Mo)O6/PVDF membrane for photocatalytic water treatment *J. Mater. Sci.* **56** 16339–50

[32] Zaaba N I, Foo K L, Hashim U, Tan S J, Liu W W and Voon C H 2017 Synthesis of graphene oxide using modified hummers method: solvent influence *Proc. Eng.* **184** 469–77

[33] Guo C, Li N, Qian X, Shi J, Jing M, Teng K and Xu Z 2020 Ultra-thin double Janus nanofiltration membrane for separation of Li + and Mg^{2+}: 'Drag' effect from carboxyl-containing negative interlayer *Sep. Purif. Technol.* **230** 115567

[34] Wu J, Yuan L, Li Z, Xie X and Huang Y 2020 Air-stable means more: designing air-defendable lithium metals for safe and stable batteries *Mater. Horiz.* **7** 2619–34

[35] Hakimi M and Alikhani M 2020 Characterization of α-Fe_2O_3 nanoparticles prepared from a new [Fe(Ofloxacin)2Cl^2] precursor: a heterogeneous photocatalyst for removal of methylene blue and ciprofloxacin in water *J. Inorg. Organomet. Polym. Mater.* **30** 504–12

[36] Ullah H, Tahir A A and Mallick T K 2018 Structural and electronic properties of oxygen defective and Se-doped p-type $BiVO_4$(001) thin film for the applications of photocatalysis *Appl. Catal.* B **224** 895–903
[37] Momma K and Izumi F 2011 VESTA3 for three-dimensional visualization of crystal, volumetric and morphology data *J. Appl. Crystallogr.* **44** 1272–6
[38] Toby B H and Von Dreele R B IUCr 2013 GSAS-II: the genesis of a modern open-source all purpose crystallography software package **46** 544–9
[39] Shang M, Wang W, Ren J, Sun S and Zhang L 2010 A novel $BiVO_4$ hierarchical nanostructure: controllable synthesis, growth mechanism, and application in photocatalysis *CrystEngComm* **12** 1754
[40] Ahmad R, Kim J K, Kim J H and Kim J 2017 Nanostructured ceramic photocatalytic membrane modified with a polymer template for textile wastewater treatment *Appl. Sci.* **7** 1284
[41] Wang L, Zhang S, Wu S, Long Y, Li L, Zheng Z, Hei Y, Zhou L, Luo L and Jiang F 2020 Controlling wettability of $AgI/BiVO_4$ composite photocatalyst and its effect on photocatalytic performance *J. Alloys Compd.* **835** 155367
[42] Feng B, Xu K and Huang A 2017 Synthesis of graphene oxide/polyimide mixed matrix membranes for desalination *RSC Adv.* **7** 2211–7
[43] Kim S W, Kim H K, Yun J W, Kim E J and Hahn S H 2015 Wetting and photocatalytic properties of TiO_2 nanotube arrays prepared via anodic oxidation of E-beam evaporated Ti thin films *Int. J. Photoenergy* **1** 6